applied sciences

MDPI

Article

Theoretical Investigation for Angle Measurement Based on Femtosecond Maker Fringe

Kuangyi Li, Wijayanti Dwi Astuti, Ryo Sato, Hiraku Matsukuma * and Wei Gao

Precision Nanometrology Laboratory, Department of Finemechanics, Tohoku University, Sendai 980-8579, Japan; li.kuangyi.t3@dc.tohoku.ac.jp (K.L.); astuti.wijayanti.s2@dc.tohoku.ac.jp (W.D.A.); ryo.sato.t5@dc.tohoku.ac.jp (R.S.); i.ko.c2@tohoku.ac.jp (W.G.)

* Correspondence: hiraku.matsukuma.d3@tohoku.ac.jp; Tel.: +81-022-795-6953

Abstract: This paper proposes to utilize a femtosecond Maker fringe for angular measurement to expand the measurement range by using the characteristic of the multiple visible peaks in the Maker fringe. Four different z-cut nonlinear materials and three different polarization combinations of SHG were considered in the study, and various theoretical results are calculated for both the intensity-based angle measurement and the frequency-domain angle measurement. As a result, the p-s polarization shows a significant angle dependence in the range of $\pm 20^{\circ}$ compared with the other polarization. In addition, the BBO and KDP are superior to the other investigated materials because of the relatively higher sensitivity and visibility. The refractive index difference was introduced in this paper, and it was applied to explain the angle measurement performance of the Maker fringe successfully.

Keywords: angle measurement; second harmonic generation; Maker fringe; intensity-based angle measurement; frequency-domain angle measurement

Citation: Li, K.; Astuti, W.D.; Sato, R.; Matsukuma, H.; Gao, W. Theoretical Investigation for Angle Measurement Based on Femtosecond Maker Fringe. *Appl. Sci.* **2022**, *12*, 3702. https://doi.org/10.3390/app12073702

Academic Editors: Jerzy A. Sładek, Ksenia Ostrowska and Adam Gąska

Received: 14 March 2022
Accepted: 5 April 2022
Published: 6 April 2022

1. Introduction

The angle is a fundamental element for defining the objects in the manufacturing process [1], and it is crucial in industry to evaluate the angular displacement using a fast and accurate method. In these years, optical measurement techniques have gained widespread attention and played an essential role in the measurement field because of their inherited noncontact, high-efficiency, and ultraprecision advantages. The optical encoder is one of the most well-used sensors for the angle measurement of the rotational shaft [2]. The encoder consists of a stationary read head and a scale disk mounted on the shaft. The read head detects the change of optical signal and records the rotational angle displacement as the shaft rotates, and the measurement range can generally cover the full 360°. The precise measurement of a small angle is also significant, such as the tilt angle of the spindle in the machine tool [3]. Many optical measurement techniques can be engaged for small-angle measurements, including autocollimation and interferometry-based angular measurement [4–7]. The autocollimation utilizes the internal-reflection effect for the angle measurement [8], and the typical interferometer for angular measurement is based on the effect of small angles on interference light intensity [9]. Differing from the encoder, they do not require a disk, and only a reflector needs to be mounted on the measured object. Accordingly, the measurement setup is more flexible, and thus they are also used for the flatness measurement [10], straightness measurement [11,12], and the position measurement for a multiaxis system [13–16].

In recent decades, angle measurement techniques have generally used the monochromatic laser due to its high intensity and excellent directionality compared with the lamp or light emitting diode (LED). With the progress of laser techniques, the pulse laser source was conceived and constructed, and the pulse duration developed from nanosecond to femtosecond. The femtosecond laser, also referred to as optical frequency combs, has both the advantages of the monochromatic laser and two significant features. One is

that the ultra-short pulse contains a number of equally-spaced stable discrete modes in the frequency domain, and the other is the high peak intensity. Because of the multiple frequency modes, many research works have been made so far in length and distance measurement [17–20]. Recently, the femtosecond laser was also used in the optical angle measurement field, and some optical angle sensors were proposed and realized, such as the optical level. The optical level is based on the diffraction dispersion effects of optical frequency combs to produce an "angle scale comb" [21]. Specifically, after passing through the Fabry-Pérot etalon, the femtosecond laser beam is projected into the refractive-type diffraction grating, generating a series of first-order diffracted beams where each optical mode corresponds to a single diffracted direction. The grating is mounted on the rotary stage, and the detector is stationary. The observed mode is different as the stage rotates, and the detected intensity changes accordingly. Meanwhile, a similar concept, the mode-locked femtosecond laser collimator, has been proposed to expand the measurement range of conventional monochromatic laser collimator [22,23]. Compared with the optical level, the measurement sensitivity of the femtosecond laser collimator is not affected by the distance between the detector and the grating. Therefore, it can realize a more compact setup to conserve space. To further improve the sensitivity and visibility, the angle measurement in the frequency domain was proposed by employing the collimator objective, single-mode fiber, and spectrometer [24]. In this case, the mode can be observed clearly, and the visibility can almost arrive at 100%.

On the other hand, the high peak intensity of the femtosecond laser generates a strong electrical field, which can produce various nonlinear optical phenomena, such as the second harmonic generation (SHG) [25]. It is well-known that the SHG process is closely related to propagation direction in the nonlinear crystals, and the brilliant angle dependence of the output intensity of the second harmonic wave was found in 1962 [26]. In our previous works, the angle dependence of SHG was utilized to design sensors for the detection of angular displacement. There are two types of angular measurement solutions based on SHG that were designed and verified, including the intensity-based angular measurement and the optical frequency domain angular measurement [27,28]. The intensity-based measurement is based on the angle dependence of the generated second harmonic wave (SHW). The output intensity of SHW is maximized only when the femtosecond laser propagates along the phase-matching angle in nonlinear materials [29]. As the laser gradually rotates away from the phase-matching angle, the generated SHW degrades rapidly, and then the angular displacement can be determined according to the intensity change. The basic principle of optical frequency domain angle measurement is based on the dispersion effects of the nonlinear crystal. Due to the refractive index dispersion, the phase-matching angle of each mode in the femtosecond laser pulse is different. Therefore, the different optical frequency modes reach their intensity peaks as the femtosecond laser rotates. Intuitively, the intensity peak shifts in the optical frequency domain as the angle changes, and thus the angular displacement can be measured according to the peak shift of SHW in the frequency domain.

However, the angle dependence of SHG not only exists in the phase-matching condition but also can be observed in the phase-mismatching area [30,31]. The angle dependence in the phase-mismatching area is called the "Maker fringe" because the experimental results were first measured by Maker [26]. The incident angle dependence of the Maker fringe can even reach the range of $\pm 80^{\circ}$ in some materials [32], and thus it has a huge potential to expand the angular measurement range and improve measurement sensitivity. Differing from our previous work, the analytical model for the Maker fringe is more complex because the effects of the crystal boundary, the cut way of the crystal, and the azimuth of the measurement should be taken into account [30,33]. Therefore, the theoretical investigation of angular measurement based on the Maker fringe should be done before the experimental setup design.

This study investigates the angle dependence of the Maker fringe for both the intensity-based and the optical frequency domain angle measurement. The fundamental measure-

ment principles and the calculation model are briefly introduced for understanding. Compared with our previous research work, the Maker fringe could have multiple visible peaks as the incident angle changes. Therefore, the measurement range can be primarily expanded in expectation. In the calculation analysis, several z-cut negative uniaxial nonlinear materials and different polarizations of Maker fringe have been considered. For the intensity-based method, we discussed the effects of dispersion and refractive index on angle measurement and calculated the visibility and sensitivity. The simulation also verified several peak shifts in the optical frequency domain, and we used the central wavelength to denote the peak shift. Then, we showed the angle dependence of the central wavelength, and the measurement sensitivity was also calculated for the investigation. The contour map of the refractive index was introduced, and the results show that the refractive index is closely related to the measurement sensitivity.

2. The Theory and Principle of Angle Measurement Based on the Maker Fringe

2.1. The Principle of Angle Measurement Based on the Maker Fringe

Figure 1a shows the measurement schematic of the angular sensor based on second harmonic generation. The mode-locked femtosecond laser beam, as the incident fundamental wave (FW), induces the second harmonic wave in the nonlinear crystal, and then the transmitted SHW is detected by the optical spectrum analyzer (OSA) with a photodiode array for the fast measurement. For clarity, the transmitted FW is not shown in this figure. The X-Y-Z is the laboratory coordinate system, and the X-Z plane is parallel to the incident plane. The measurement target is fixed with the nonlinear crystal. As the target rotates along the Y-axis, the transmitted intensity of the SHW changes accordingly because of the angle dependence of the Maker fringe. Figure 1b,c show the diagram of the spectrum of incident FW and transmitted SHW, where the λ_1 and λ_2 denote the wavelength of incident FW and the transmitted SHW. The FW and SHW contain a series of equally-spaced modes in the optical frequency domain, and the frequency difference between the discrete modes of FW and SHW are ν_{rep} and $2\nu_{rep}$. Both the FW and SHW have N modes, and the ith mode of FW corresponds to the ith mode of SHW. λ_1^i and λ_2^i denote the wavelength of the ith mode of FW and SHW, and $\lambda_1^i/2 = \lambda_2^i$, that is to say that the wavelength of the generated SHW is half of the corresponding mode of FW. The intensity $I_2(\lambda_2, \theta_i)$ of transmitted SHW is both related to the wavelength λ_2 and the incident angle θ_i because of the dispersion and the angle dependence of SHG, and it can be calculated analytically by the Maker fringe theory introduced in the next section.

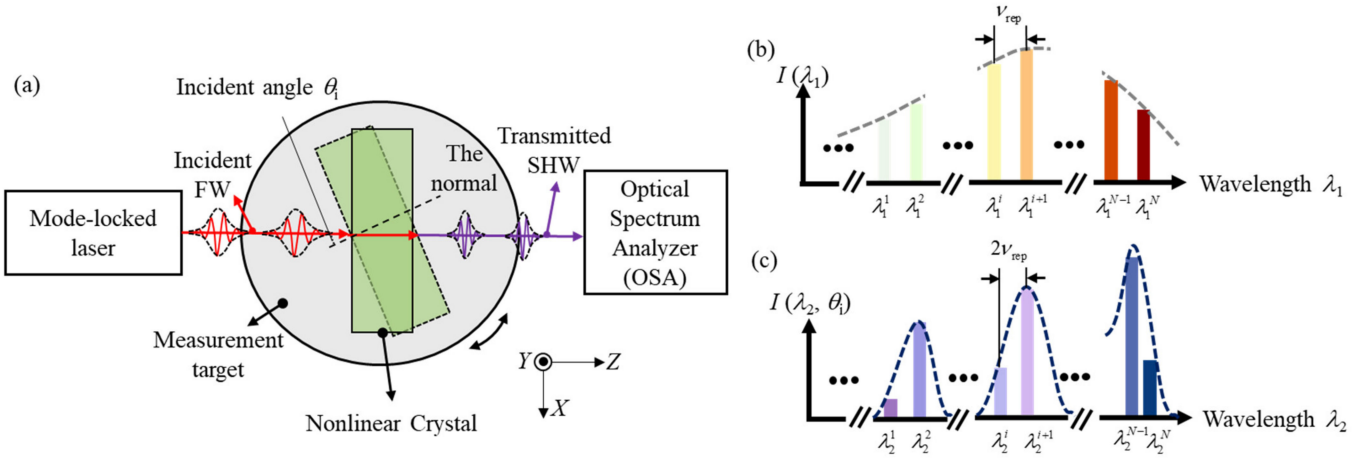

Figure 1. (**a**) The schematic of angle measurement based on SHG; (**b**) the spectrum of incident femtosecond laser; (**c**) the spectrum of transmitted SHW.

For the intensity-based angular measurement of the Maker fringe, the total intensity of all the modes in the SHW spectrum is used as the measurement signal to improve the

signal–noise ratio [26]. The total intensity I_{SHW} denotes the intensity summation of the transmitted second harmonic wave of all the discrete modes as shown in Equation (1):

$$I_{SHW}(\theta_i) = \sum_{\lambda_2^1}^{\lambda_2^N} I_2(\lambda_2, \theta_i) \quad (1)$$

where λ_2^1 and λ_2^N represent the wavelength of the first and the final mode in the SHW spectrum. The typical angle dependences of the Maker fringe and the case nearing the phase-matching condition of our previous study are shown in Figure 2a,b, where the Maker fringe has more visible peaks, which means that a wider measurement range is used.

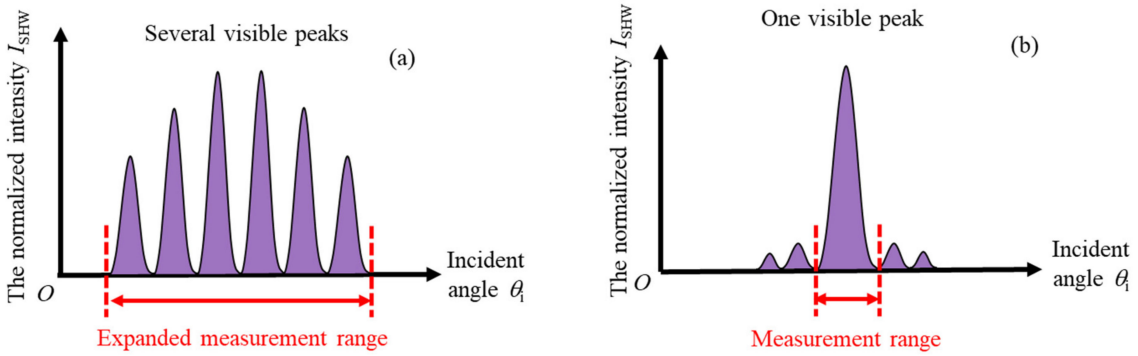

Figure 2. (**a**) The typical angle dependence of the Maker fringe; (**b**) the angle dependence nearing the phase-matching condition.

On the other hand, the Maker fringe also can be applied to the angular measurement in the optical frequency domain [27]. Figure 3a,b illustrate the peak shift in the optical frequency domain of the Maker fringe and the phase-matching case. Because of the wavelength dependence of $I_2(\lambda_2, \theta_i)$, the modes λ_2^i ($i = 1, 2, \ldots, N$) have different angle dependence relationships. Therefore, as the modes' wavelength gradually increases in the optical domain, the peaks shift in a certain speed and direction in the optical domain, and the peak shift can use to denote the angular displacement [27]. The Maker fringe has multiple visible peaks, and each peak has its shift in the frequency domain. Thus, the measurement range in the optical frequency domain can also be largely expanded.

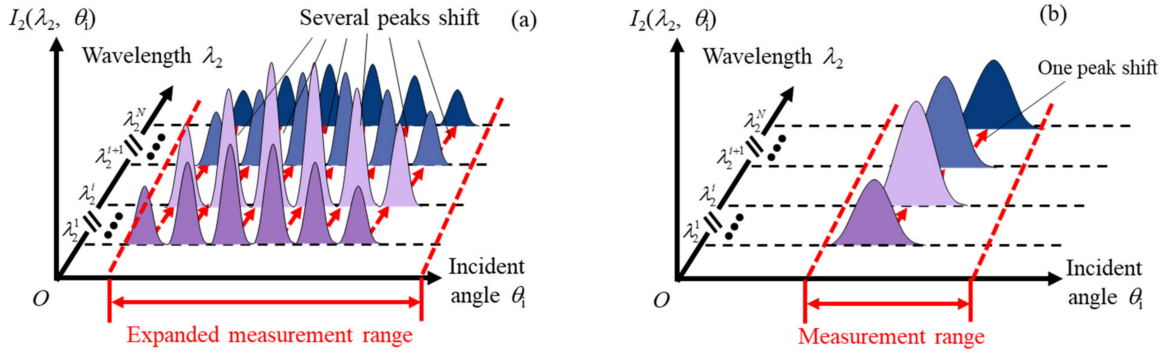

Figure 3. (**a**) The peak shifts of Maker fringe; (**b**) the peak shift nearing the phase-matching condition.

2.2. The Calculation Theory of the Maker Fringe

To quantificationally investigate the angle dependence of the Maker fringe, the calculation theory of the Maker fringe should be explained in detail. The theory of the Maker fringe is different from that of our previous works because the incident angle of the Maker fringe can vary in a wider range, where the internal reflection and refraction caused by the boundary should be considered. The propagation model proposed by the literature

is referred to calculate I_2 in this paper [29]. The model is illustrated in Figure 4a, where X'-Y'-Z' and L denote the Cartesian coordinator and the length of the rotary crystal. In this model, the incident FW inputs on the cut plane from the Region I (air), and then induces two different SHW (the bound SHW and free SHW) inside the Region II (crystal). The two SHW waves can pass through the crystal as transmitted SHW in Region III (air), and they also result in the reflected SHW in the Region I (air). The $\boldsymbol{k}_1$, $\boldsymbol{k}_b$, $\boldsymbol{k}_f$, $\boldsymbol{k}_r$, and $\boldsymbol{k}_t$ are the wave vectors of the fundamental wave, bound SHW, free SHW, reflected SHW, and transmitted SHW, respectively. Correspondingly, the θ_i, θ_b, θ_f, θ_r, and θ_t are the angles between the wave vectors and the normal. For calculation, the incident angle θ_i is a known parameter, and the other angles in Figure 4a should be calculated. It can be derived by considering the conservation of the electrical field's tangential component and the result is shown as Equation (2) [34]:

$$\theta_i = \theta_r = \theta_t = n_b \sin\theta_b = n_f \sin\theta_f \tag{2}$$

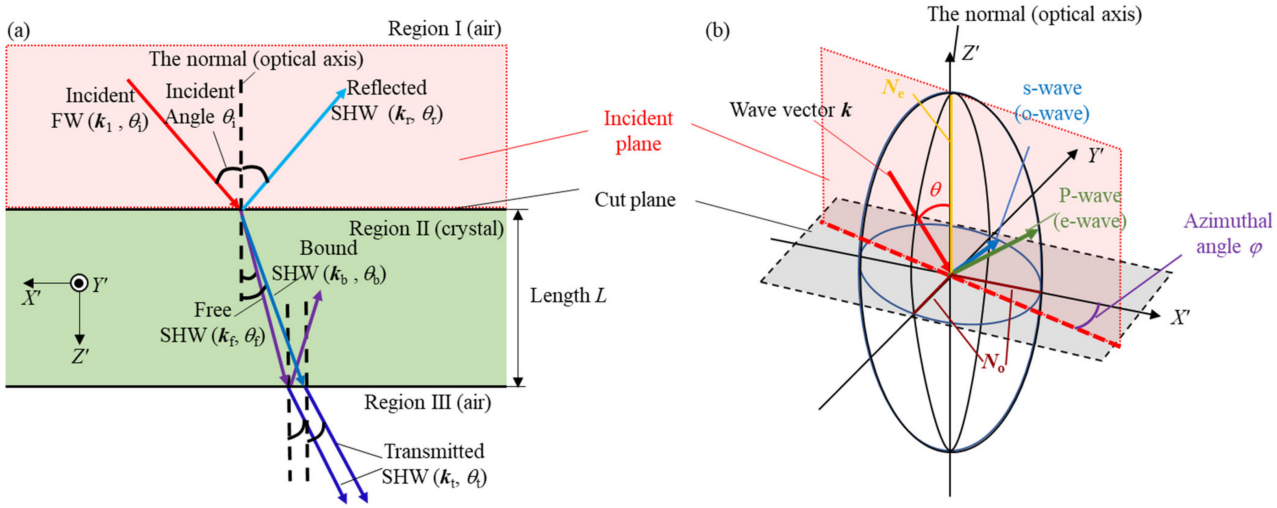

Figure 4. (**a**) The propagation model in the incident plane; (**b**) the refractive index ellipsoid.

Equation (2) shows that θ_b and θ_f are related to the refractive indices of the bound SHW (n_b) and the free SHW (n_f). In this paper, we assume that the optic axis is parallel to the norm to simplify the analysis. That is to say that the z-cut nonlinear crystal is used for the investigation, and the coordinator of the refractive index ellipsoid is the same as X' -Y' -Z' . For the commonly used uniaxial crystal, the refractive index ellipsoid is shown in Figure 4b [35]. The N_o and N_e are the length of a refractive ellipsoid, and their dispersion could be described by empirical Sellmeier equations [36]. The θ denotes the angle between the optical axis and the wave vector $\boldsymbol{k}$, and φ denotes the azimuthal position between the X' axis and the projection of wave vector $\boldsymbol{k}$ in the X' -Y' plane. For the z-cut crystal, the s-wave or the o-wave represents the wave whose electrical field is perpendicular to the incident plane. The electrical field of the p-wave or the e-wave is parallel to the incident plane. According to their polarization, the refractive index of s-wave and p-wave can be calculated as Equation (3):

$$\begin{aligned} n_{b,f}(\lambda, \theta_{b,f}) &= \frac{1}{\sqrt{\left(\cos^2(\theta_{b,f})/N_o^2(\lambda_{1,2}) + \sin^2(\theta_{b,f})/N_e^2(\lambda_{1,2})\right)}} \text{ p-wave} \\ n_{b,f} &= N_o(\lambda_{1,2}) \text{ s-wave} \end{aligned} \tag{3}$$

where λ_1 and λ_2 correspond to the wavelength of the fundamental wave and second harmonic wave in a vacuum. Since the velocity of bound SHW is the same as the FW, the corresponding wavelength for n_b is λ_1, and λ_2 is for n_f of free SHW. Once the refractive index has been determined, the propagation direction of all waves can be obtained using Snell's law in Equation (2), and then the intensity I_2 of transmitted SHW can be known

by solving the Maxwell equation and considering the boundary condition. With the assumptions of plane wave and the pump nondepletion, I_2 is proportional to the production of Equation (4) [29], where t_1, t_2 are the transmission factors of FW and SHW, I_1 is the intensity of FW, d_{eff} is the effective nonlinear coefficient, and ψ is the phase difference between bound SHW and free SHW in Equation (5).

$$I_2 \propto d_{\text{eff}}^2 t_1^4 t_2 I_1^2(\lambda_1)[1/(n_b^2 - n_f^2)^2] \sin^2 \psi \tag{4}$$

$$\psi = [2\pi L/\lambda_1(n_b \cos\theta_b - n_f \cos\theta_f)] \tag{5}$$

$$t_1 = \begin{cases} 2\cos\theta/(n_b \cos\theta_b + \cos\theta) \text{ s-wave} \\ 2\cos\theta/(n_b \cos\theta + \cos\theta_b) \text{ p-wave} \end{cases} \tag{6}$$

$$t_2 = \begin{cases} 2n_f \cos\theta_f \frac{(n_b \cos\theta + \cos\theta_b)(n_f \cos\theta_b + n_b \cos\theta_f)}{(n_f \cos\theta_f + \cos\theta)^3} \text{ s-wave} \\ 2n_f \cos\theta_f \frac{(\cos\theta + n_b \cos\theta_b)(n_b \cos\theta_b + n_f \cos\theta_f)}{(n_f \cos\theta_f + \cos\theta)^3} \text{ p-wave} \end{cases} \tag{7}$$

The transmission factors t_1 and t_2 represent the effects caused by the boundary of the nonlinear crystal. Thus, they are similar to Fresnel factors, and their values are related to the polarization of the fundamental wave and second harmonic wave as Equations (6) and (7). There are four different polarization combinations of SHG, including s-s case, s-p case, p-s case, and p-p case. For example, the s-p case implies that the incident s-polarization FW induces the p-polarization transmitted SHW, which means that the second harmonic wave may have a different polarization from the fundamental wave. The transmission factor has slowly varying angle dependence, which should be considered in the expanded angle measurement range calculation. Besides this, the effective nonlinear coefficient d_{eff} also has slowly varying angle dependence, and the calculation should refer to the point groups of crystal and polarization combination of SHG [28]. In Section 3, the paper gives extensive calculation results based on this model for two different measurement principles, including the intensity-based angular measurement and the optical frequency domain measurement.

3. Simulation Results and Discussion

3.1. The Simulation Setup

Figure 5 shows the typical spectrum of femtosecond laser from our previous work, and it is used as the fundamental wave for the angle dependence investigation. The spectrum range of the fundamental wave is from 1480 nm to 1640 nm, meaning that the generated SHW will have a distribution from 740 nm to 820 nm. In the calculation process, the spectrum of the femtosecond laser is divided into a number of laser combs. For each comb, we assume it produces a corresponding mode of transmitted SHW, and the intensity of each mode can be calculated by Equation (4).

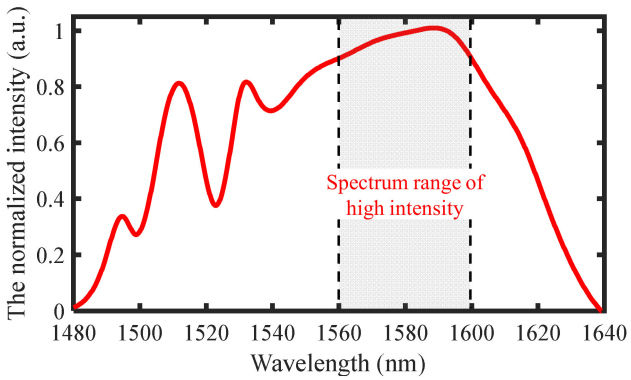

Figure 5. The spectrum of a femtosecond laser used for the angular measurement investigation; the spectrum range of high intensity is from 1560 nm to around 1600 nm.

The investigated materials include barium borate (BBO), lithium niobate ($LiNbO_3$), potassium dihydrogen phosphate (KDP), and proustite (Ag_3AsS_3), which are both negative uniaxial crystals. The Sellmeier equations given in Equation (8) are used to empirically describe the dispersion relation of nonlinear materials, where the parameters A, B, C, D, E are related to the specific materials. The coefficients for refractive indices calculation are shown in Table 1 [35].

$$\begin{aligned} N_e(\lambda), N_o(\lambda) &= \sqrt{A + \frac{B}{\lambda^2 - C} - D\lambda^2}\ \text{BBO}\ LiNbO_3 \\ N_e(\lambda), N_o(\lambda) &= \sqrt{A + \frac{B\lambda^2}{\lambda^2 - C} - \frac{D}{\lambda^2 - E}}\ \text{KDP} \\ N_e(\lambda), N_o(\lambda) &= \sqrt{A + \frac{B}{\lambda^2 - C} - \frac{D}{\lambda^2 - E}}\ Ag_3AsS_3 \end{aligned} \tag{8}$$

Table 1. The parameters of the Sellmeier equation for the calculation of refractive indices.

Nonlinear Crystal	*A*	*B*	*C*	*D*	*E*
BBO					
N_o	2.7539	0.01878 μm^2	0.01822 μm^2	0.01354 μm^{-2}	*
N_e	2.3753	0.01224 μm^2	0.01667 μm^2	0.01516 μm^{-2}	
$LiNbO_3$					
N_o	4.91296	0.116275 μm^2	0.048398 μm^2	0.0273 μm^{-2}	
N_e	4.54528	0.091649 μm^2	0.046079 μm^2	0.0303 μm^{-2}	
KDP					
N_o	2.259276	13.005221	400 μm^2	0.01008956 μm^2	$(77.26408)^{-1}$ μm^2
N_e	2.132668	3.22799241	400 μm^2	0.008637494 μm^2	$(81.42631)^{-1}$ μm^2
Ag_3AsS_3					
N_o	9.220	0.4454 μm^2	0.1264 μm^2	1733 μm^2	1000 μm^2
N_e	7.007	0.3230 μm^2	0.1192 μm^2	660 μm^2	1000 μm^2

* The '\' means that the Sellmeier equations of BBO and $LiNbO_3$ aren't related to parameter E.

The angle dependence of the transmitted second harmonic wave also should consider the effective nonlinear coefficients d_{eff}. For the SHG process, the d_{eff} of the crystals are decided based on their point groups and the polarization combinations. The derivation of d_{eff} could refer to the literature [28], and d_{eff} are directly given in Table 2, where the dispersion and the walk-off effects of d_{eff} are ignored. There are three polarization combinations, the p-s case, p-p case, and s-s case, which will be discussed, with the exclusion of the s-p case. This is because the s-p case denotes that the s-polarization fundamental wave generates the p-polarization, and it means that the ordinary fundament wave generates the extraordinary second harmonic wave, which is the phase-matching case discussed in our previous works [26]. Therefore, the s-p case will not be investigated in this paper. The BBO, $LiNbO_3$, and Ag_3AsS_3 have a 3 m point group structure, except that the KDP belongs to the $\bar{4}2$ m point group. Thus, the KDP is the only one with a different d_{eff} distinguished from the others. Table 2 lists the nonlinear coefficients for all materials according to the references [35], and it is important to note that the nonlinear coefficients are different even for the same point group structure materials.

Table 2. The effective nonlinear coefficients d_{eff} of the investigated nonlinear crystals.

Point Group	Nonlinear Crystal	Effective Nonlinear Coefficient			Nonlinear Coefficient
		p-s Case	p-p Case	s-s Case	
3 m	BBO $LiNbO_3$ Ag_3AsS_3	$d_{22}\cos\theta\cos3\varphi$	$d_{31}(\cos\theta\sin2\theta + \cos^2\theta\sin\theta) + d_{22}\cos^3\theta\sin3\varphi$	$d_{22}\cos3\varphi$	d_{22} = 2.3 pm/v d_{31} = −0.16 pm/v d_{22} = 2.1 pm/v d_{31} = −4.35 pm/v d_{22} = 10.4 pm/v d_{31} = −16.6 pm/v
$\bar{4}2$ m	KDP	$d_{36}\sin2\theta\cos2\varphi$	$d_{36}(\sin2\theta\cos\theta\sin2\varphi + \cos^2\theta\sin2\varphi)$	0	d_{36} = 0.39 pm/v

3.2. The Investigation of Intensity-Based Angle Measurement

To investigate the intensity-based method, Figure 6 displays the results of the incident angle dependence of the transmitted second harmonic wave. The total intensity I_{SHW} denotes the summation of all the discrete light combs as Equation (1). The azimuthal angle φ and the crystal length L are set as 0° and 1 mm for the calculation. In each subplot, the incident angle range is in the range of ±20°, and all the curves are normalized. The subplot and the color represent the results of the crystals and the polarization combinations. It can be seen that all the curves in Figure 6 show an angle dependence in the range of ±20°. The p-s polarization of BBO and KDP show significant measurement visibility and sensitivity because of the oscillation of angle dependence. In comparison, the oscillation of the p-s polarization of the $LiNbO_3$ is subtle, and the Ag_3AsS_3 does not appear to oscillate, which also means they are not suitable for intensity angle measurement. The visibility V and the averaged sensitivity S can be calculated according to the following equation:

$$V = \frac{I_{max} - I_{min}}{I_{max} + I_{min}} \tag{9}$$

$$S = \frac{I_{max} - I_{min}}{\Delta\theta} \tag{10}$$

where I_{max} and I_{min} denote the maximum intensity and the minimum intensity in one oscillation period, and $\Delta\theta$ denote the angle difference in one oscillation period [23]. The visibility and sensitivity are calculated for the BBO and KDP as shown in Figure 6. For the BBO, the visibility and measurement sensitivity in the shown oscillation period are about 25.1% and 0.08/deg, respectively. For the KDP, the visibility and sensitivity are 69.2% and 0.35/deg.

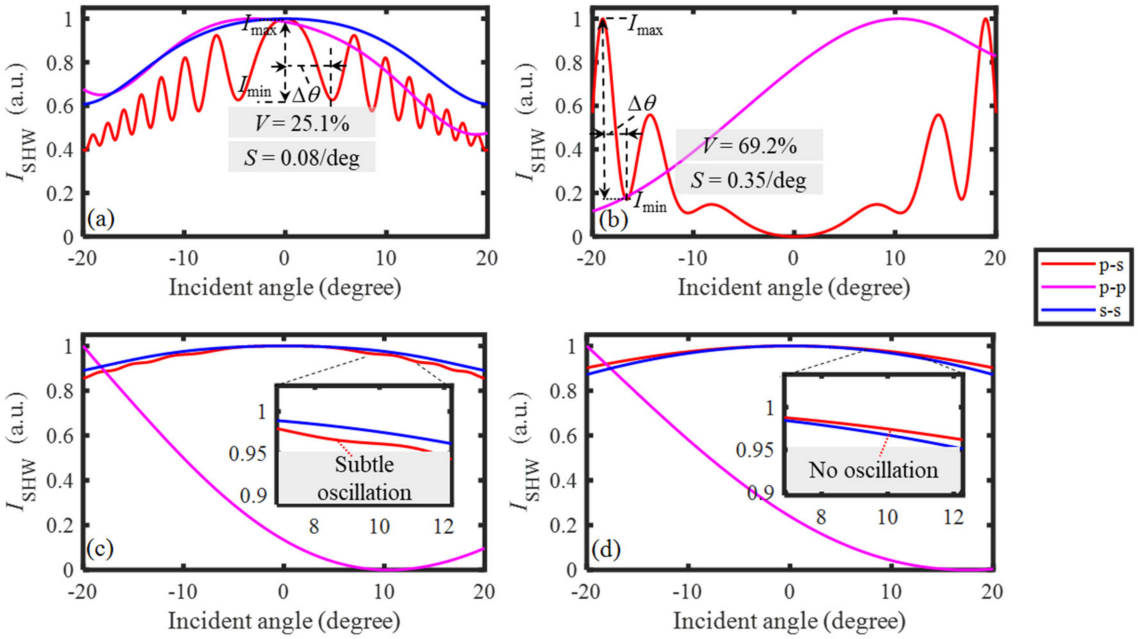

Figure 6. The angular dependence of the total intensity of the second harmonic wave. (**a**) BBO; (**b**) KDP; (**c**) $LiNbO_3$; (**d**) Ag_3AsS_3.

The visibility and measurement sensitivity of p-s polarization are closely related to the dispersion of the material. To be intuitive, Figure 7 shows the angle dependence of different discrete light modes. In this figure, the light combs take the wavelengths of 1560 nm, 1570 nm, and 1580 nm, respectively, and the calculation results are given for all the crystals in each corresponding subplot. It can be seen that the KDP has the lowest dispersion. Thus, the oscillations of the different optical combs are more likely to cancel

out, which is advantageous for improving both the sensitivity and the visibility of angular measurement. In contrast, the Ag_3AsS_3 has a fast dispersion, and it causes the oscillation of angle dependence to disappear, as Figure 6d illustrated.

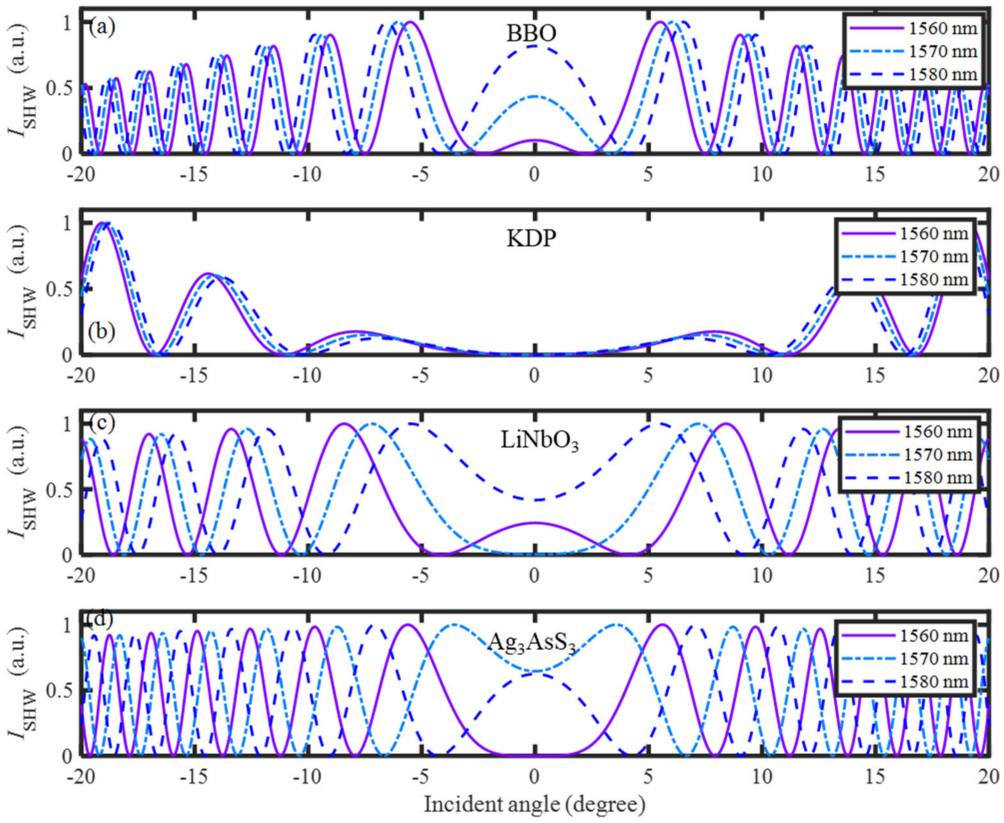

Figure 7. The dispersion of angle dependence. (**a**) BBO; (**b**) KDP; (**c**) $LiNbO_3$; (**d**) Ag_3AsS_3.

Furthermore, it also can be noticed from Figure 6 that neither the p-p case nor the s-s case shows any oscillation in the angle dependence, which also means low measurement sensitivity and visibility. This is because the oscillation is related to the angle dependence of phase difference ψ in Equation (5). The more sensitive the angle dependence of the ψ is, the shorter the period of the oscillation will be, i.e., the better the sensitivity and visibility of the angular measurement. We note that the phase difference is proportional to the term as Equation (11), which is determined by the refractive index difference Δn as (12):

$$\psi \propto (n_\mathrm{b} \cos\theta_\mathrm{b} - n_\mathrm{f} \cos\theta_\mathrm{f}) \tag{11}$$

$$\Delta n = n_\mathrm{b} - n_\mathrm{f} \tag{12}$$

Figure 8 exhibits the angle dependence of Δn for the light comb of 1560 nm, where the different lines in each subplot denote the polarization combinations, and the subplots correspond to the materials. It is clear that the angle dependence of the Δn of p-s polarization is much faster than that of the p-p polarization and s-s polarization for all the nonlinear materials, and it leads to rapid changes in phase difference ψ and thus the rapid oscillations of the intensity. Therefore, the p-s polarization combination is more appropriate for the angular measurement for the z-cut nonlinear crystals.

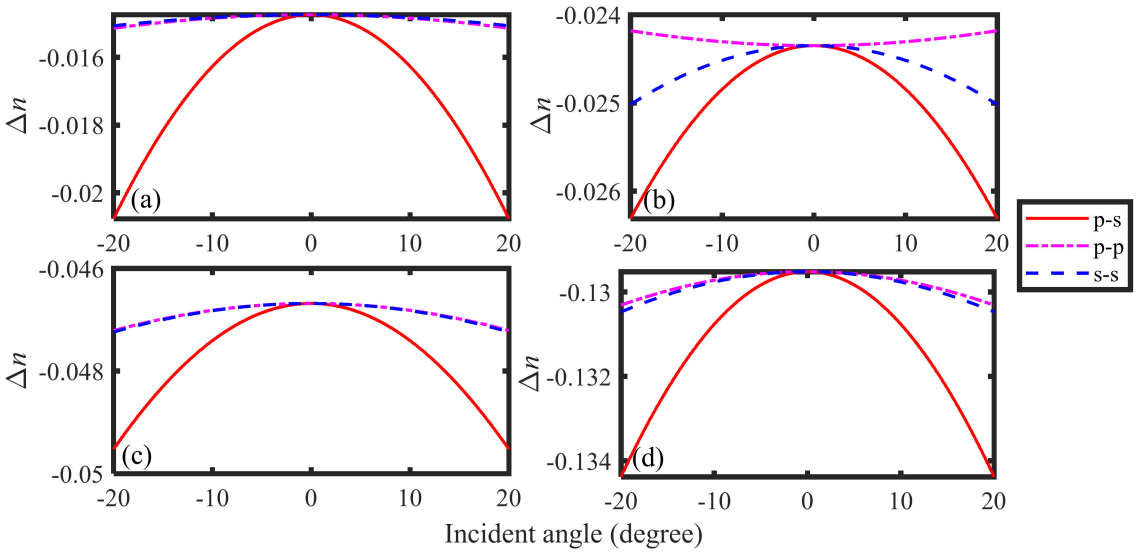

Figure 8. The angular dependence of the refractive indices difference Δn. (**a**) BBO; (**b**) KDP; (**c**) $LiNbO_3$; (**d**) Ag_3AsS_3. The red solid lines, pink dotted lines, and blue dotted lines in each subplot represent the p-s polarization, p-p polarization, and the s-s polarization, respectively.

In addition to the visibility and sensitivity, the absolute magnitude of SHW intensity is also significant. It is evident from Equation (4) that the larger the d_{eff}, the greater the measured intensity. Therefore, the proper azimuthal position φ should be set in the measurement process. For the p-s polarization, it is easy to see from Table 2 that the d_{eff} reaches its maximum value when $\varphi = 0$ because of the cosine dependence. The d_{eff} also affects the symmetry of the angle dependence. As shown in Figure 6, all the angle dependence of p-p polarization is not symmetrical because the d_{eff} of p-p polarization in this paper consists of two terms, one of which is an odd function and the other is an even function. In addition, there is a particular case in Table 2 in which the d_{eff} of the s-s case of KDP does not have any angle dependence. This means that an s-polarization incident femtosecond laser cannot produce an s-polarization second harmonic wave in a z-cut KDP, and thus the angle dependence of this case is not shown in Figure 6b.

3.3. The Investigation of Angle Measurement in the Optical Frequency Domain

Figure 9 takes the p-s polarization of $LiNbO_3$ as a typical example to show the Maker fringe shift in the optical domain. The azimuthal position and the length are set as 0° and 1 mm for the calculation. The 2-D result can be seen Figure 9a, where the color bar represents the normalized intensity. The incident angle range is from 0° to 20°, and the spectral range is from 740 nm to around 820 nm, corresponding to half the wavelength of the FW's spectrum. There are several peaks of maker fringe shift shown in Figure 9a as the white arrow shown in the white dotted square. It can be seen that all the peaks move towards longer wavelengths as the incident angle increase, and the higher intensity areas are 780 nm to around 800 nm in the optical frequency domain, which is correlated with the higher intensity light combs of FW. The 3-D plot of peak shift in the range of 5 to around 20° is illustrated in Figure 9b, where the modes are from 780 nm to 800 nm and stepped by 2 nm. It is visible that the six peaks of Maker fringe change their peak position in the optical domain, and all the peak shifts could be used to measure the angular displacement. In Figure 9a, these peaks cover the range of 0° to around 20° in 780 nm to around 800 nm. Therefore, the maker fringe can realize an angular measurement range of ±20° only with a bandwidth of 20 nm (only the result of 0° to around 20° shown in Figure 9, and a significant savings of the femtosecond laser bandwidth can achieve this, compared with our previous study [27]).

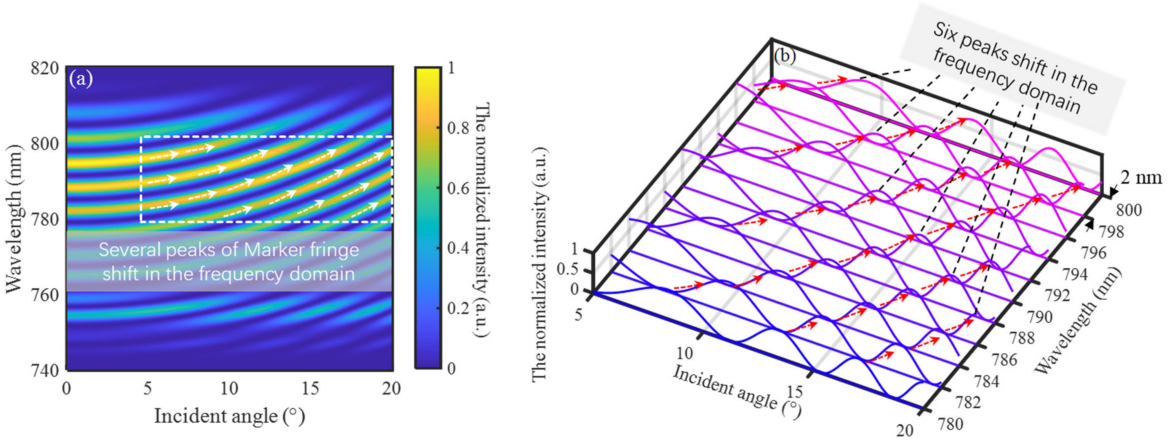

Figure 9. The Maker fringe shift of p-s polarization of $LiNbO_3$. (**a**) The 2D plot; (**b**) 3D plot in the higher intensity area.

For further analysis, the materials in Table 1 are both investigated. The φ and L are set as 25° and 1 mm, and the calculation results are shown in Figure 10, where the (a), (b), (c), (d) indicate the nonlinear materials BBO, KDP, $LiNbO_3$, and Ag_3AsS_3 in order, the numbers 1, 2, 3 denote the polarization combinations p-s, p-p, and s-s, respectively. In each subplot, the discussed incidence angle range is from 0° to 20°, and the spectral range is from 780 nm to 800 nm because of the higher intensity. The s-s polarization of KDP is not given in Figure 10 because of the corresponding $d_{\text{eff}} = 0$ in Table 1. We notice that all the subplots have at least one peak shift, and the peaks almost cover the whole measurement range of interest. Besides this, it is easy to find that the shape of different peaks in the same subplot is similar. Thus, we only cut a single peak from every subplot to discuss its angle dependence in the frequency domain. The single peaks shift corresponding to Figure 10 is given in Figure 11. Similar to our previous work, the central wavelengths λ_p is used to illustrate the peak's wavelength in the frequency domain [27]. The calculation is given as the following formula:

$$\lambda_P(\theta_i) = \frac{\sum_{\lambda_2=780\text{nm}}^{800\text{nm}} \lambda_2 I_2(\lambda_2, \theta_i)}{\sum_{\lambda_2=780\text{nm}}^{800\text{nm}} I_2(\lambda_2, \theta_i)} \tag{13}$$

The angle dependence of λ_p of Figure 11 is shown in Figure 12. In this figure, the (a), (b), and (c) denote the subplot p-s polarization, p-p polarization, and s-s polarization, respectively, and the lines in different colors represent the corresponding material. It can be seen from Figure 12 that the peak wavelength λ_P almost monotonically increases or decreases as the incident angle changes. The slope of the angle dependence implies the measurement sensitivity. Similar to the intensity-based measurement, the averaged sensitivity S' of optical frequency domain angular measurement can be calculated as Equation (14):

$$S' = \frac{\lambda_P(\theta_{ie}) - \lambda_P(\theta_{is})}{\Delta\theta_i} \tag{14}$$

where θ_{is} and θ_{ie} denote the start and end incident angle of the λ_p's angular dependence curve, and $\Delta\theta_i = \theta_{ie} - \theta_{is}$. Taking the p-s polarization of BBO as an example, we show $\lambda_P(\theta_{is}) - \lambda_P(\theta_{ie})$ and $\Delta\theta_i$ in Figure 12a. The sensitivities S' of other cases are shown in Table 3. It is clear that the p-s polarization's sensitivity is significantly higher than the p-p polarization and s-s polarization. Therefore, the p-s polarization is superior to the other two polarization combinations for the angular measurement in the optical frequency domain. The p-s polarization of BBO has the best measurement sensitivity 1.43×10^{-3} nm/arcsecond among the investigated materials, and only the KDP has a relatively higher sensitivity of -1.01×10^{-3} nm/arcsecond.

Table 3. The averaged sensitivity of angle measurement in the optical frequency domain.

	BBO	KDP	$LiNbO_3$	Ag_3AsS_3
p-s polarization	1.43×10^{-3}	-1.01×10^{-3}	2.05×10^{-4}	1.17×10^{-4}
p-p polarization	1.11×10^{-4}	4.53×10^{-5}	5.87×10^{-5}	1.90×10^{-5}
s-s polarization	9.80×10^{-5}	\ *	5.91×10^{-5}	1.98×10^{-5}

* The unit of averaged measurement sensitivity is 'nm/arcsecond'. The '\' means that the s-s polarization of KDP doesn't have measurement sensitivity because of $d_{\text{eff}} = 0$.

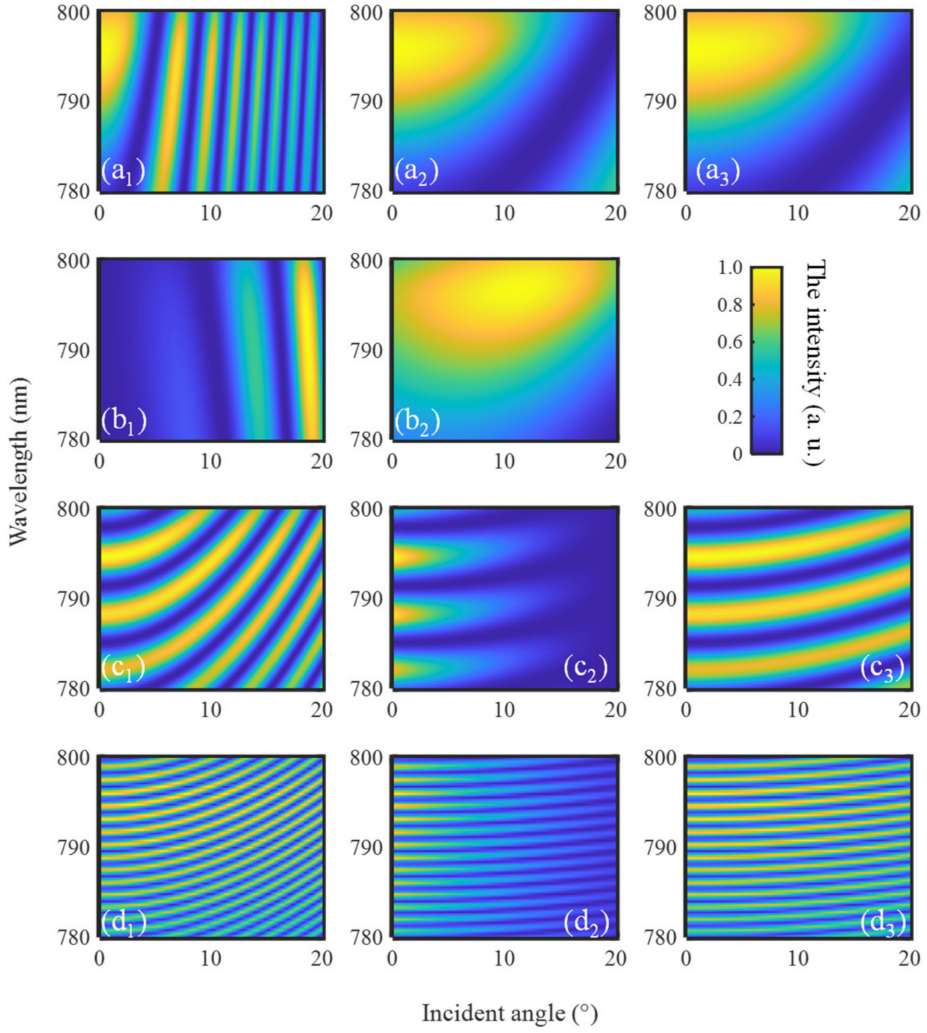

Figure 10. The calculation results of peaks shift in the optical frequency domain. The figures (**a**–**d**) denote the nonlinear materials BBO, KDP, $LiNbO_3$, and Ag_3AsS_3 in order, the subscript numbers 1, 2, 3 denote the polarization combinations p-s, p-p, and s-s, respectively.

The measurement sensitivity S' is also closely related to the phase difference ψ. This is because the peak shift is, in fact, the movement of the point where $\psi = constant$. As Equations (11) and (12), the phase difference ψ is related to the refractive index Δn. Therefore, the peak shift is determined by the point of $\Delta n = constant$. Figure 13 shows the contour map of Δn of the p-s polarization. In this figure, the subplots (a), (b), (c), and (d) correspond to the crystal BBO, KDP, $LiNbO_3$, and Ag_3AsS_3, respectively. In each subplot, the lines in different colors denote the different constants of Δn, and the step of Δn between different lines is 0.001. It is easy to understand that the higher the slope of the line, the faster the wavelength changes as the angle changes in the line, i.e., the faster the peak shift. BBO has the highest line slope compared to the others, and therefore its measurement sensitivity is the best. We note that only the KDP has a negative linear slope, which means that as the

angle increases, the wavelength should decrease to keep Δn as a constant, and it causes its negative sensitivity. In addition, the number of lines varies from different materials. The more lines mean, the greater number of peaks. Thus, the Ag_3AsS_3 has the most peaks among the discussed material.

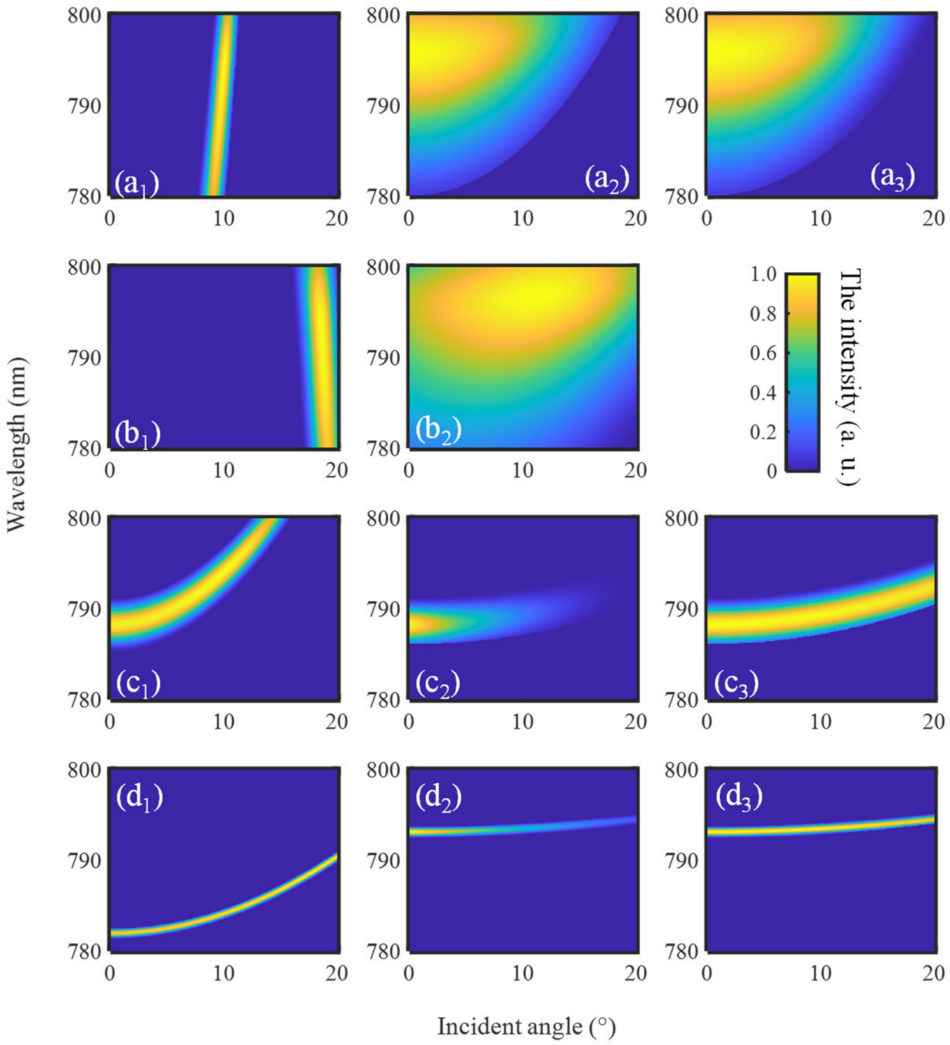

Figure 11. The calculation results of single peak shifts in the optical frequency domain. The figures (**a**–**d**) denote the nonlinear materials BBO, KDP, $LiNbO_3$, and Ag_3AsS_3 in order, the subscript numbers 1, 2, 3 denote the polarization combinations p-s, p-p, and s-s, respectively.

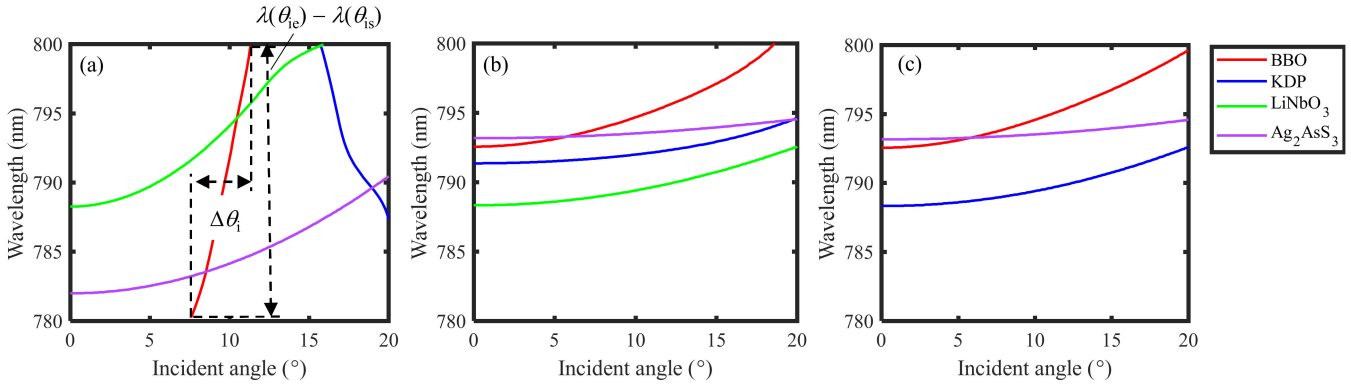

Figure 12. The angle dependence of central wavelength λ_P. (**a**) p-s polarization; (**b**) p-p polarization; (**c**) s-s polarization.

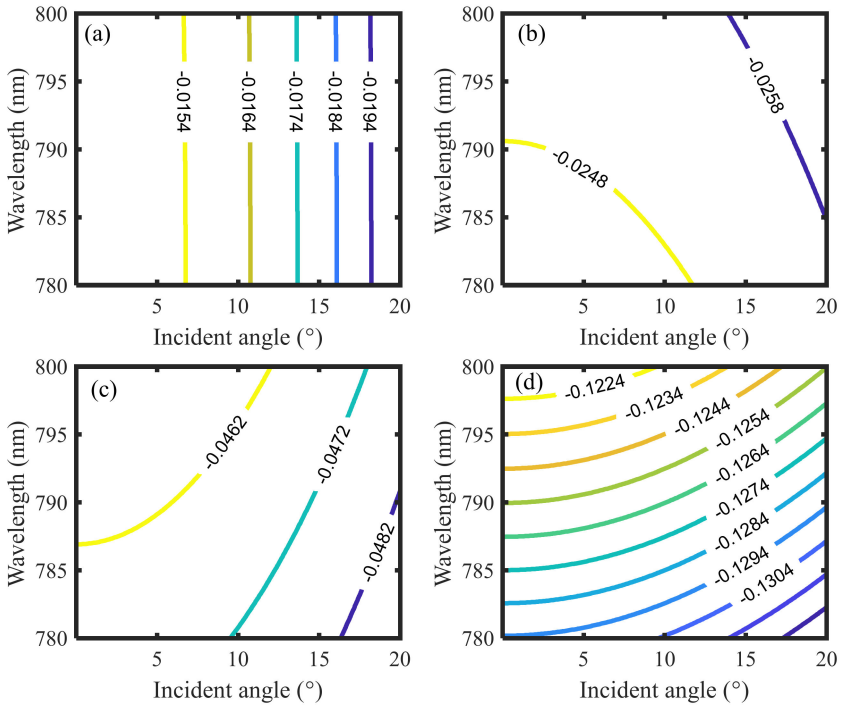

Figure 13. The contour map of Δn of the investigated materials. (**a**) BBO; (**b**) KDP; (**c**) $LiNbO_3$; (**d**) Ag_3AsS_3. In every subplot, the lines in different colors denote the different constants of Δn, and the step of Δn between different lines is 0.001.

4. Conclusions

In this paper, we propose to use the femtosecond Maker fringe for angular measurement and present various calculation results of different z-cut nonlinear crystals and polarization combinations. The calculation investigation has been done for both the intensity-based angular measurement and the optical frequency domain angular measurement.

For the intensity-based method, the calculation results show that p-p polarization and s-s polarization only has the slow varying angle dependence in the Maker fringe, which means low sensitivity and visibility. In contrast, the Maker fringe of p-s polarization has a relatively higher sensitivity and visibility because of the oscillation in the angle dependence. To explain the oscillation of the Maker fringe, the refractive index difference Δn was introduced, and the results show that the Δn's angle dependence of p-s polarization is significantly faster than the others, thus confirming the relationship between the oscillation and the Δn. Besides this, we also calculate the Maker fringe in different modes to explore the effect of dispersion and calculate the sensitivity and visibility of BBO and KDP.

As a typical case, the multiple peaks shift of Maker fringe in the optical frequency domain can be clearly seen in the p-s polarization of $LiNbO_3$, and it can cover a measurement range of $\pm 20^\circ$ only with a bandwidth of 20 nm. Moreover, we show other cases of the Maker fringe shift, and the multiple fringes can also be seen in some materials. We cut the single peak from the calculation results and used the central wavelength to denote the peak's angle dependence. The measurement sensitivity of central wavelength was calculated, and the p-s polarization of BBO has the best sensitivity of 1.43×10^{-3} nm/arcsecond. In addition, the contour map of refractive index difference Δn was used to explore the determining factor of measurement sensitivity, and the results confirmed that the slope and number of contour lines are closely related to the measurement sensitivity and the peaks' number.

It should be noted that the theoretical investigation in this paper has been mainly focused on visibility and sensitivity. However, there are many other aspects that are also important for designing a sensor in the actual application, such as measurement selectivity and stability. Taking the selectivity as an example, the Maker fringe should not only be

sensitive to incident angle θ_i but also should be insensitive to other factors that may affect the measurement, such as the azimuthal angle φ. Therefore, a comprehensive analysis will be done in future works by considering both selectivity and stability. Then, a measurement scheme will be considered to verify the feasibility of angle measurement based on the Maker fringe.

Author Contributions: Conceptualization, W.G.; methodology, W.G., H.M. and K.L.; software, K.L. and W.D.A.; formal analysis, K.L.; investigation, W.D.A. and R.S.; resources, W.G.; data curation, K.L. and H.M.; writing—original draft preparation, K.L.; writing—review and editing, H.M. and W.G.; visualization, K.L.; supervision, W.G.; funding acquisition, W.G. and H.M. All authors have read and agreed to the published version of the manuscript.

Funding: This work is supported by the Japan Society for the Promotion of Science (JSPS) 15H05759 and 20H00211.

Institutional Review Board Statement: Not applicable.

Informed Consent Statement: Not applicable.

Data Availability Statement: The data presented in this study are available on request from the corresponding author.

Acknowledgments: Li Kuangyi would like to thank the Graduate Program for Integration of Mechanical Systems (GP-Mech) of Tohoku University, Japan.

Conflicts of Interest: The authors declare no conflict of interest. The funders had no role in the design of the study; in the collection, analyses, or interpretation of data; in the writing of the manuscript, or in the decision to publish the results.

References

1. Shimizu, Y.; Matsukuma, H.; Gao, W. Optical Angle Sensor Technology Based on the Optical Frequency Comb Laser. *Appl. Sci.* **2020**, *10*, 4047. [CrossRef]
2. Gao, W.; Kim, S.W.; Bosse, H.; Haitjema, H.; Chen, Y.L.; Lu, X.D.; Knapp, W.; Weckenmann, A.; Estler, W.T.; Kunzmann, H. Measurement Technologies for Precision Positioning. *CIRP Annals* **2015**, *64*, 773–796. [CrossRef]
3. Fu, P.; Jiang, Y.; Zhou, L.; Wang, Y.; Cao, Q.; Zhang, Q.; Zhang, F. Measurement of Spindle Tilt Error Based on Interference Fringe. *Int. J. Precis. Eng. Manuf.* **2019**, *20*, 701–709. [CrossRef]
4. Shimizu, Y.; Tan, S.L.; Murata, D.; Maruyama, T.; Ito, S.; Chen, Y.-L.; Gao, W. Ultra-Sensitive Angle Sensor Based on Laser Autocollimation for Measurement of Stage Tilt Motions. *Opt. Express* **2016**, *24*, 2788. [CrossRef] [PubMed]
5. Matsukuma, H.; Asumi, Y.; Nagaoka, M.; Shimizu, Y.; Gao, W. An Autocollimator with a Mid-Infrared Laser for Angular Measurement of Rough Surfaces. *Precis. Eng.* **2021**, *67*, 89–99. [CrossRef]
6. Ge, Z.; Takeda, M. High-Resolution Two-Dimensional Angle Measurement Technique Based on Fringe Analysis. *Appl. Opt.* **2003**, *42*, 6859. [CrossRef]
7. Chen, X.; Liao, J.; Gu, H.; Zhang, C.; Jiang, H.; Liu, S. Remote Absolute Roll-Angle Measurement in Range of 180° Based on Polarization Modulation. *Nanomanuf. Metrol* **2020**, *3*, 228–235. [CrossRef]
8. Huang, P.S.; Kiyono, S.; Kamada, O. Angle Measurement Based on the Internal-Reflection Effect: A New Method. *Appl. Opt.* **1992**, *31*, 6047. [CrossRef]
9. Ehret, G.; Schulz, M.; Stavridis, M.; Elster, C. Deflectometric Systems for Absolute Flatness Measurements at PTB. *Meas. Sci. Technol.* **2012**, *23*, 094007. [CrossRef]
10. Yang, P.; Takamura, T.; Takahashi, S.; Takamasu, K.; Sato, O.; Osawa, S.; Takatsuji, T. Development of High-Precision Micro-Coordinate Measuring Machine: Multi-Probe Measurement System for Measuring Yaw and Straightness Motion Error of XY Linear Stage. *Precis. Eng.* **2011**, *35*, 424–430. [CrossRef]
11. Chen, B.; Xu, B.; Yan, L.; Zhang, E.; Liu, Y. Laser Straightness Interferometer System with Rotational Error Compensation and Simultaneous Measurement of Six Degrees of Freedom Error Parameters. *Opt. Express* **2015**, *23*, 9052. [CrossRef] [PubMed]
12. Cui, C.; Feng, Q.; Zhang, B. Compensation for Straightness Measurement Systematic Errors in Six Degree-of-Freedom Motion Error Simultaneous Measurement System. *Appl. Opt.* **2015**, *54*, 3122. [CrossRef] [PubMed]
13. Li, X.; Gao, W.; Muto, H.; Shimizu, Y.; Ito, S.; Dian, S. A Six-Degree-of-Freedom Surface Encoder for Precision Positioning of a Planar Motion Stage. *Precis. Eng.* **2013**, *37*, 771–781. [CrossRef]
14. Gao, S.; Zhang, B.; Feng, Q.; Cui, C.; Chen, S.; Zhao, Y. Errors Crosstalk Analysis and Compensation in the Simultaneous Measuring System for Five-Degree-of-Freedom Geometric Error. *Appl. Opt.* **2015**, *54*, 458. [CrossRef]
15. Matsukuma, H.; Ishizuka, R.; Furuta, M.; Li, X.; Shimizu, Y.; Gao, W. Reduction in Cross-Talk Errors in a Six-Degree-of-Freedom Surface Encoder. *Nanomanuf. Metrol.* **2019**, *2*, 111–123. [CrossRef]

16. Huang, P.; Li, Y.; Wei, H.; Ren, L.; Zhao, S. Five-Degrees-of-Freedom Measurement System Based on a Monolithic Prism and Phase-Sensitive Detection Technique. *Appl. Opt.* **2013**, *52*, 6607. [CrossRef]
17. Bloembergen, N. Nonlinear Optics: Past, Present, and Future. *IEEE J. Sel. Top. Quantum Electron.* **2000**, *6*, 5. [CrossRef]
18. Udem, T.; Holzwarth, R.; Hänsch, T.W. Optical Frequency Metrology. *Nature* **2002**, *416*, 5. [CrossRef]
19. Schuhler, N.; Salvadé, Y.; Lévêque, S.; Dändliker, R.; Holzwarth, R. Frequency-Comb-Referenced Two-Wavelength Source for Absolute Distance Measurement. *Opt. Lett.* **2006**, *31*, 3101. [CrossRef]
20. Jin, J.; Kim, Y.-J.; Kim, Y.; Kang, C.-S.; Kim, S.-W. Absolute Length Calibration of Gauge Blocks Using Optical Comb of a Femtosecond Pulse Laser. *Opt. Express* **2006**, *14*, 5968–5974. [CrossRef]
21. Shimizu, Y.; Kudo, Y.; Chen, Y.-L.; Ito, S.; Gao, W. An Optical Lever by Using a Mode-Locked Laser for Angle Measurement. *Precis. Eng.* **2017**, *47*, 72–80. [CrossRef]
22. Chen, Y.-L.; Shimizu, Y.; Kudo, Y.; Ito, S.; Gao, W. Mode-Locked Laser Autocollimator with an Expanded Measurement Range. *Opt. Express* **2016**, *24*, 15554. [CrossRef] [PubMed]
23. Chen, Y.-L.; Shimizu, Y.; Tamada, J.; Nakamura, K.; Matsukuma, H.; Chen, X.; Gao, W. Laser Autocollimation Based on an Optical Frequency Comb for Absolute Angular Position Measurement. *Precis. Eng.* **2018**, *54*, 284–293. [CrossRef]
24. Chen, Y.-L.; Shimizu, Y.; Tamada, J.; Kudo, Y.; Madokoro, S.; Nakamura, K.; Gao, W. Optical Frequency Domain Angle Measurement in a Femtosecond Laser Autocollimator. *Opt. Express* **2017**, *25*, 16725. [CrossRef] [PubMed]
25. Thomson, R.; Leburn, C.; Reid, D. *(Eds). Ultrafast Nonlinear Optics*; Springer International Publishing: Heidelberg, Gremany, 2013; ISBN 978-3-319-00016-9.
26. Maker, P.D.; Terhune, R.W.; Nisenoff, M.; Savage, C.M. Effects of Dispersion and Focusing on the Production of Optical Harmonics. *Phys. Rev. Lett.* **1962**, *8*, 21–22. [CrossRef]
27. Matsukuma, H.; Madokoro, S.; Astuti, W.D.; Shimizu, Y.; Gao, W. A New Optical Angle Measurement Method Based on Second Harmonic Generation with a Mode-Locked Femtosecond Laser. *Nanomanuf. Metrol.* **2019**, *2*, 187–198. [CrossRef]
28. Dwi Astuti, W.; Matsukuma, H.; Nakao, M.; Li, K.; Shimizu, Y.; Gao, W. An Optical Frequency Domain Angle Measurement Method Based on Second Harmonic Generation. *Sensors* **2021**, *21*, 670. [CrossRef]
29. Powers, P.E.; Haus, J.W. *Fundamentals of Nonlinear Optics*, 2nd ed.; CRC Press Taylor & Francis: Boca Raton, FL, USA, 2017; ISBN 978-1-4987-3683-1.
30. Jerphagnon, J.; Kurtz, S.K. Maker Fringes: A Detailed Comparison of Theory and Experiment for Isotropic and Uniaxial Crystals. *J. Appl. Phys.* **1970**, *41*, 1667–1681. [CrossRef]
31. Heisler, I.A.; Misoguti, L.; Zílio, S.C.; Rodriguez, E.V.; de Araújo, C.B. Spectrally Resolved Femtosecond Maker Fringes Technique. *Appl. Phys. Lett.* **2008**, *4*, 091109. [CrossRef]
32. Park, D.H.; Herman, W.N. Closed-Form Maker Fringe Formulas for Poled Polymer Thin Films in Multilayer Structures. *Opt. Express* **2012**, *20*, 173. [CrossRef]
33. Herman, W.N.; Hayden, L.M. Maker Fringes Revisited: Second-Harmonic Generation from Birefringent or Absorbing Materials. *JOSA B* **1995**, *12*, 416–427. [CrossRef]
34. Bloembergen, N.; Pershan, P.S. Light Waves at the Boundary of Nonlinear Media. *Phys. Rev.* **1962**, *128*, 606–622. [CrossRef]
35. ShunXiang, S. *Nonlinear Optics*; Xidian University Press: Xi'an, China, 2012.
36. Dmitriev, V.G.; Gurzadyan, G.G.; Nikogosyan, D.N. *Handbook of Nonlinear Optical Crystals*; Springer Series in Optical Sciences; Springer: Berlin/Heidelberg, Germany, 1999; Volume 64, ISBN 978-3-642-08472-0.